Cross section measurement for the ^{10}B(n,$t2\alpha$) three-body reaction at 4.0, 4.5, and 5.0 MeV. I. Prediction of the experimental spectrum

Zhimin Wang,[1,2] Huaiyong Bai,[1] Luyu Zhang,[1] Haoyu Jiang,[1] Yi Lu,[1] Jinxiang Chen,[1] Guohui Zhang,[1,*] Yu. M. Gledenov,[3] M. V. Sedysheva,[3] and G. Khuukhenkhuu[4]

[1]*State Key Laboratory of Nuclear Physics and Technology, Institute of Heavy Ion Physics, Peking University, Beijing 100871, China*

[2]*Department of Physics, School of Information Science and Engineering, Ocean University of China, Qingdao 266100, China*

[3]*Frank Laboratory of Neutron Physics, Joint Institute for Nuclear Research, Dubna 141980, Russia*

[4]*Nuclear Research Centre, National University of Mongolia, Ulaanbaatar 17032, Mongolia*

(Received 29 June 2017; published 24 October 2017)

Cross sections of the ^{10}B(n,$t2\alpha$) three-body reaction were measured at $E_n = 4.0$,4.5, and 5.0 MeV using a twin gridded ionization chamber and a thin-film ^{10}B sample. The present paper is the first part of the work. The experimental spectrum of the ^{10}B(n,$t2\alpha$) reaction measured by the gridded ionization chamber (GIC) was predicted. The ^{10}B(n,$t2\alpha$) reaction can proceed in three ways, which are referred to as ^{7}Li**, ^{8}Be, and breakup channels. The energies and directional angles of the three particles in the final states for the ^{7}Li**, ^{8}Be, and breakup channels were calculated, respectively. Based on these results, the one-dimensional and two-dimensional spectra were calculated through integration. Three kinds of interference reactions were taken into account, which were the ^{10}B(n,α)^{7}Li reaction, the H(n, n)p reaction, and the (n,α) reactions from the working gas of the GIC. Two effects were considered in the prediction of the experimental spectrum, which were the energy loss of the products in the sample and the wall effect of the sample position well. The predicted spectra play an important role in the guidance of the implementation of the experiment and the processing of the experimental data.

DOI: 10.1103/PhysRevC.96.044620

I. INTRODUCTION

As is well known, the ^{10}B isotope is widely used in neutron detection, reactor control and shielding protection, and many other applications. The main nuclear reaction of the ^{10}B isotope induced by thermal and epithermal neutrons is the ^{10}B(n,α)^{7}Li reaction and its cross sections are inversely proportional to the neutron velocity (the $1/v$ law). In the MeV energy region, cross sections of the ^{10}B(n,$t2\alpha$) three-body reaction increase rapidly and become larger than those of the ^{10}B(n,α)^{7}Li two-body reaction at about 4.5 MeV.

Experimental studies on the ^{10}B(n,$t2\alpha$) three-body reaction were carried out just a few years after the discovery of the neutron [1,2]. To date, four kinds of detection methods have been employed to measure this reaction: boron-loaded emulsion [1–3], tritium counting [4,5], the ΔE-E counter telescope [6,7], and the gridded ionization chamber (GIC) [8,9]. However, large discrepancies exist among the experimental cross section data. In particular, cross sections measured by the GIC detector are significantly lower than those measured with other methods. The shapes of the excitation functions are also different from each other. Both the magnitude and the trend of GIC measured results are not adopted by the evaluated data libraries.

In both of the existing measurements using the GIC detector, a ^{10}B gas sample was used [8,9]. The chamber was filled with a mixture of Kr (or Ar) and BF_3 gas. When the gas sample is used, much attention should be paid to the wall effect of the GIC detector, whereby the reaction products would leave the region of uniform electric field or collide with the electrodes of the chamber. The wall effect would result in a major uncertainty of event counting and the number of target nuclei.

To avoid the wall effect, we propose to measure the ^{10}B(n,$t2\alpha$) reaction using a ^{10}B solid sample deploying into a twin gridded ionization chamber. The ^{10}B sample should be very thin, so both the forward and backward emitted particles from the three-body reaction could come out of the sample and be detected simultaneously by the chamber. The total energy of each three-body event can be obtained by the summation of the amplitudes of the forward and backward signals. From the total-energy spectrum, the ^{10}B(n,$t2\alpha$) reaction events could be distinguished from those of the ^{10}B(n,α)^{7}Li reaction because of the difference of the Q values. The Q values of the ^{10}B(n,$t2\alpha$) and ^{10}B(n,α)^{7}Li reactions are 0.323 and 2.790 MeV, respectively (corresponding to the ground state of the residual nucleus). In additino to the total-energy spectrum, the forward and backward spectra, which contain more dynamic information than the Q value of the reaction, can also be measured.

In order to be able to implement the coincidence measurement of the ^{10}B(n,$t2\alpha$) three-body reaction according to the above experimental scheme, three things need to be done: (1) theoretical prediction of the experimental spectrum of the ^{10}B(n,$t2\alpha$) reaction measured by the GIC detector, (2) development of the GIC spectrometer based on a waveform digitizer (WFD), and (3) preparation of a thin-film ^{10}B sample and determination of the number of ^{10}B atoms. The present paper shows the prediction of the experimental spectrum. The WFD-based GIC spectrometer and the thin-film ^{10}B sample, as well as the experimental results of the ^{10}B(n,$t2\alpha$) reaction, are presented in the second paper [10].

*Corresponding author: guohuizhang@pku.edu.cn

TABLE I. The level schemes of ^{7}Li and ^{8}Be isotopes [12].

	^{7}Li		^{8}Be	
	E_k (MeV)	$J\pi$	E_k (MeV)	$J\pi$
Ground state	0	3/2−	0	0+
First level	0.478	1/2−	3.030	2+
Second level	4.630	7/2−	11.350	4+
Third level	6.680	5/2−	16.626	2+
Fourth level	7.459	5/2−		

II. THE ^{10}B(n,$t2\alpha$) REACTION AND EXPERIMENTAL SPECTRUM

The ^{10}B(n,$t2\alpha$) reaction, leading to one triton and two α particles in the final state, can proceed in three ways as follows [8]:

$$^{10}\mathrm{B} + n \rightarrow {}^{7}\mathrm{Li}^{**} + \alpha - 1.840\ \mathrm{MeV},$$
$$^{7}\mathrm{Li}^{**} \rightarrow \alpha + t + 2.162\ \mathrm{MeV}, \quad (1)$$
$$^{10}\mathrm{B} + n \rightarrow {}^{8}\mathrm{Be} + t + 0.230\ \mathrm{MeV},$$
$$^{8}\mathrm{Be} \rightarrow \alpha + \alpha + 0.092\ \mathrm{MeV}, \quad (2)$$
$$^{10}\mathrm{B} + n \rightarrow \alpha + \alpha + t + 0.322\ \mathrm{MeV}. \quad (3)$$

Mechanisms (1) and (2) take place through a chain of two-body processes with ^{7}Li and ^{8}Be as the intermediate nuclei, respectively. There is a strong α-t final-state interaction in mechanism (1) and α-α interaction in mechanism (2). Mechanism (3) proceeds as a three-body breakup of the compound nucleus of ^{11}B. This is a pure kinematic process without interaction between the three particles in the final state. Hereafter, mechanisms (1)–(3) are referred to as ^{7}Li**, ^{8}Be, and breakup channels, respectively.

The two superscript stars in the name of mechanism (1), i.e., the ^{7}Li** channel, indicate that the intermediate nucleus ^{7}Li is at the second or higher excited levels. If ^{7}Li is at the first excited level, it will decay through γ deexcitation to the ground state; this leads to the ^{10}B(n,α)^{7}Li two-body reaction. For the ^{8}Be nucleus, it is not stable at either ground or excited states, and it will decay spontaneously into two α particles. The discrete level schemes of ^{7}Li and ^{8}Be are shown in Table I. In fact, the above phenomenon shows one of the characteristics of the neutron induced light-nucleus reaction. Different levels of the intermediate residual nucleus may belong to different reaction channels due to the different decay modes from these levels [11].

In view of the particle emission mechanism for the neutron induced reactions of the 1p-shell nucleus (from ^{6}Li up to ^{16}O), all of the emission processes proceed between discrete levels. Meanwhile, in addition to the equilibrium mechanism, the preequilibrium emission process becomes prominent and must be taken into account [13]. Therefore, the key point to describe the neutron induced light-nucleus reaction is that the conservation of parity and angular momentum should be considered properly in the preequilibrium emission process. A unified Hauser-Feshbach and exciton model was proposed by

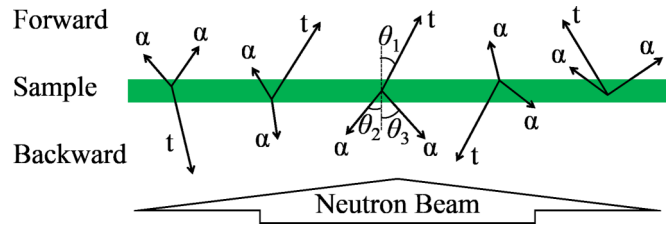

FIG. 1. The representative emission situations of the three particles in the final state for the ^{10}B(n,$t2\alpha$) reaction.

Zhang *et al.* [14]. The master equation theory of precompound and compound nuclear reactions was generalized to include the conservation of parity and angular momentum. Based on this improved model, they developed the LUNF code to calculate the neutron induced reaction data for ^{6}Li, ^{7}Li, ^{9}Be, ^{10}B, ^{11}B, ^{12}C, ^{14}N, and ^{16}O isotopes. The cross sections and the double-differential cross sections of the ^{10}B(n,$t2\alpha$) three-body reaction can be calculated by the LUNF code.

Since the double-differential cross sections of the three products from the ^{10}B(n,$t2\alpha$) reaction are calculated individually in the LUNF code, they could not be used to predict the experimental spectrum measured by the GIC. In the present measurement, the triton and α particle cannot be distinguished by the GIC detector; thus, the spectrum of the triton or α particle cannot be obtained individually. The forward and backward spectra measured by the GIC [15] are the superposition of all of the partial spectra corresponding to the different emission situations of the three particles as shown in Fig. 1. The forward or backward directions may contain one, two, or even three particles.

All the emission situations of the three particles constitute the final-state phase space of the ^{10}B(n,$t2\alpha$) reaction. In the numerical calculation, the final-state phase space is discretized; in other words, it consists of many phase-space bins. Different bins corresponds to different emission situations as shown in Fig. 1. Each phase-space bin, referred to as $\delta_i()$, is described by the energy ε and the directional angle Ω (θ and φ) of each of the three particles. With the complete final-state phase space, the forward and backward spectra of the ^{10}B(n,$t2\alpha$) reaction can be obtained by superimposing the spectra of all of the phase-space bins. In addition, the energy loss of the products in the sample and the wall effect of the sample position well [16] need to be taken into account. Therefore, the experimental forward and backward spectra S_{fb} can be calculated by the following equation:

$$S_{fb} = \sum_i p_i F(\delta_i(m_1,\varepsilon_1,\theta_1,\varphi_1;m_2,\varepsilon_2,\theta_2,\varphi_2;m_3,\varepsilon_3,\theta_3,\varphi_3;)), \quad (4)$$

where p_i is the state density of each phase-space bin and $F()$ refers to the correction operations of the energy loss and the wall effect of the sample position well. Details about the correction methods of the energy loss and the wall effect of the sample position well can be found in Refs. [15,16], respectively.

The key point to predict the experimental spectrum is to calculate the complete final-state phase-space of the ^{10}B(n,$t2\alpha$) reaction. The calculation method for the sequential two-body

process, namely, the ^{7}Li** and ^{8}Be channels, is different from that for the three-body breakup process. The two calculation methods are introduced in Secs. III and IV, respectively. Section V shows the interference reactions which contain the ^{10}B$(n,\alpha)^{7}$Li reaction, the H(n, n)p reaction, and the (n,α) reactions of the working gas from the GIC. The predicted spectra are given in Sec. VI. Section VII shows the conclusions.

III. CALCULATION METHOD FOR THE ^{7}Li** AND ^{8}Be CHANNELS

In general, the calculation process of the final-state phase-space for the ^{7}Li** and ^{8}Be channels consists of four steps. First, the angular distribution of the first emitted particle in the center-of-mass system (CMS) is calculated by the LUNF code. The first emitted particle is an α particle in the ^{7}Li** channel and a triton in the ^{8}Be channel as shown in Eqs. (1) and (2), respectively. Second, the energy and angle of the second emitted particle are calculated in the recoil nucleus system (RNS). The RNS is a moving system that is set at the end of the velocity vector of the recoil residual nucleus in the CMS. Third, the energy and angle of the second emitted particle are transformed from the RNS to the CMS. Finally, the energy and angle of the first and second emitted particles are transformed from the CMS to the laboratory system (LS). Three motion systems are used and the physical quantities in the present paper are indicated by the superscripts L, C, and R for the LS, CMS, and RNS systems, respectively. In this section, the ^{7}Li** channel is to be taken as the example to introduce the calculation process.

In the LUNF code, the angular distribution of the first emitted particle in the sequential two-body process is given by the Legendre coefficients representation as follows:

$$\sigma(\cos\theta^{\mathrm{C}},\phi^{\mathrm{C}}) \equiv \frac{d\sigma}{d\Omega^{\mathrm{C}}} = \frac{1}{4\pi}\sum_{l}(2l+1)f_l P_l(\cos\theta^{\mathrm{C}}), \quad (5)$$

where f_l is the Legendre coefficients and $P_l()$ are the Legendre polynomials. Here the value of l is from zero to 5 and the f_0 is normalized to the total cross section. Quantities $\cos\theta^{C}$ and φ^{C} are discretized in the numerical calculation.

Using Eq. (5), the angular distribution of the first emitted particle $\sigma(\cos\theta_{\alpha}^{C},\varphi_{\alpha}^{C})$ for the ^{7}Li** channel is obtained. Then, according to the conservation of energy and momentum, the energy of the first emitted particle ε_{α}^{C}, and the energy and angular distribution of the intermediate nucleus ^{7}Li, $E_{7\mathrm{Li}}^{C}$, and $\sigma(\cos\theta_{7\mathrm{Li}}^{C},\varphi_{7\mathrm{Li}}^{C})$, can be calculated by the following equations:

$$\begin{aligned}
\varepsilon_{\alpha}^{\mathrm{C}} &= \frac{M_{7\mathrm{Li}}}{m_{\alpha}+M_{7\mathrm{Li}}}E_{\mathrm{tot}}^{\mathrm{C}},\\
E_{7\mathrm{Li}}^{\mathrm{C}} &= \frac{m_{\alpha}}{m_{\alpha}+M_{7\mathrm{Li}}}E_{\mathrm{tot}}^{\mathrm{C}},\\
E_{\mathrm{tot}}^{\mathrm{C}} &= \frac{M_{10\mathrm{B}}}{M_{10\mathrm{B}}+m_n}E_n^{\mathrm{L}} + Q_1 - E_{7\mathrm{Li}}^{**},\\
\sigma\left(\cos\theta_{7\mathrm{Li}}^{\mathrm{C}},\phi_{7\mathrm{Li}}^{\mathrm{C}}\right) &= \sigma\left(-\cos\theta_{\alpha}^{\mathrm{C}},\phi_{\alpha}^{\mathrm{C}}+\pi\right), \qquad (6)
\end{aligned}$$

where $m_{\alpha}, M_{7\mathrm{Li}}, m_n,$, and $M_{10\mathrm{B}}$ are the masses of the α particle, ^{7}Li, the neutron, and the ^{10}B nucleus, respectively; E_n^{L} is the incident neutron energy in the LS; Q_1 is the reaction energy which is -1.840 MeV as shown in Eq. (1); $E_{7\mathrm{Li}}^{**}$ is the second excitation energy of ^{7}Li; and E_{tot}^{C} is the total kinetic energy of the α particle and ^{7}Li in the CMS. (Note that if the ^{7}Li nucleus is at the third excitation energy, then Q_1 is equal to -3.890 MeV and E_{tot}^{C} is the third excitation energy of ^{7}Li.) Using Eqs. (5) and (6), the energy and directional angles of the first emitted particle and the ^{7}Li nucleus are obtained.

It is assumed that the angular distribution of the second particle is isotropic in the RNS [13,17]. Using energy and momentum conservation, the following equations are derived for the energy and angular distribution of the second particle in the RNS:

$$\begin{aligned}
\varepsilon_{\alpha'}^{\mathrm{R}} &= \frac{m_t}{M_{7\mathrm{Li}}}(Q_2 + E_{7\mathrm{Li}}^{**}),\\
\varepsilon_{t}^{\mathrm{R}} &= \frac{m_{\alpha}}{M_{7\mathrm{Li}}}(Q_2 + E_{7\mathrm{Li}}^{**}), \qquad (7)\\
\sigma\left(\cos\theta_{\alpha'}^{\mathrm{R}},\phi_{\alpha'}^{\mathrm{R}}\right) &= \sigma\left(-\cos\theta_{t}^{\mathrm{R}},\phi_{t}^{\mathrm{R}}+\pi\right) = \frac{1}{4\pi},
\end{aligned}$$

where Q_2 is the reaction energy, which is 2.162 MeV as shown in Eq. (1). (If the ^{7}Li nucleus is at the third excitation energy, then Q_2 is equal to 4.212 MeV.) The other parameters have the same meaning as those in Eq. (6).

Next, we need to transform the energy and angular distribution of the second emitted particle from the RNS to the CMS. Here the key point is that the transformation is related not only to the polar angle θ, but also to the azimuthal angle φ, because the RNS has not only translational motion but also the rotational motion in the CMS. This question can be understood clearly in the coordinate frames of the RNS, CMS, and LS shown as the x''-y''-z'', x'-y'-z', and x-y-z frames, respectively, in Fig. 2.

As is the common practice, the z axis of the LS is along the direction of the velocity vector of the incident neutron and the CMS starts from the end of the velocity vector of the center of mass in the LS, i.e., $\overrightarrow{V_{\mathrm{c.m.}}^{\mathrm{L}}}$. Therefore, the z' axis of the CMS is coincident with the z axis of the LS as shown in Fig. 2. The x and y axes of the LS and CMS are set according to the rule of the right-handed coordinate system. For the RNS coordinate, the z'' axis is along the direction of the velocity vector of the recoil nucleus ^{7}Li in the CMS, i.e., $\overrightarrow{V_{\mathrm{Li}}^{\mathrm{C}}}$. The y'' axis of the RNS is set in the plane which is perpendicular to the x'-y' plane of the CMS coordinate frame and contains the velocity vector $\overrightarrow{V_{\mathrm{Li}}^{\mathrm{C}}}$. The x'' axis of the RNS is set according to the rule of the right-handed coordinate system. It can be proved that the x'' axis of the RNS is in the x'-y' plane of the CMS. The proof is as follows: the x'' axis is perpendicular to the y''-z'' plane and the z' axis is in the y''-z'' plane, thus the x'' axis is perpendicular to the z' axis; the z' axis is perpendicular to the x'-y' plane and the origin of the x'' axis is in the x'-y' plane, so the x'' axis is in the x'-y' plane. As can be seen below, the properties of the above coordinate frames make it easy to rotate the frame from the RNS to the CMS.

The transformation from the RNS to the CMS for the energy and angular distribution of the second emitted particles includes two steps. The first step is to transform the velocity vector $\overrightarrow{V_{\alpha'}^{\mathrm{R}}}$ to $\overrightarrow{V_{\alpha'}^{\mathrm{C}}}$ as shown in Fig. 2. The transformation

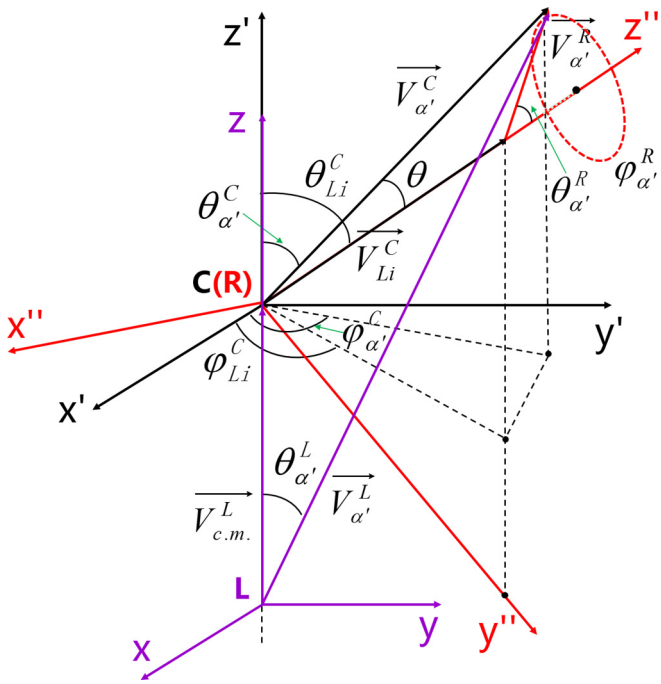

FIG. 2. The relationship of the velocity vector between the RNS (x''-y''-z''), CMS (x'-y'-z'), and LS (x-y-z) for the second-emitted α particle from the ^{7}Li** channel.

approach is the same as that for the common transformation from the CMS to the LS using the method of velocity composition. The transform equations for the energy, angle, and angular distribution are as follows:

$$\begin{aligned}
\varepsilon^{\mathrm{C}}_{\alpha'} &= \varepsilon^{\mathrm{R}}_{\alpha'}\left(1+\gamma^2+2\gamma\cos\theta^{\mathrm{R}}_{\alpha'}\right),\\
\cos\theta^{\mathrm{C}}_{\alpha'} &= \frac{\gamma+\cos\theta^{\mathrm{R}}_{\alpha'}}{\sqrt{1+\gamma^2+2\gamma\cos\theta^{\mathrm{R}}_{\alpha'}}},\\
\frac{d\sigma}{d\Omega^{\mathrm{C}}_{\alpha'}} &= \frac{d\sigma}{d\Omega^{\mathrm{R}}_{\alpha'}}\frac{\left(1+\gamma^2+2\gamma\cos\theta^{\mathrm{R}}_{\alpha'}\right)}{\left|1+\gamma\cos\theta^{\mathrm{R}}_{\alpha'}\right|},\\
\gamma &\equiv \frac{\left|\vec{V}^{\mathrm{C}}_{\mathrm{Li}}\right|}{\left|\vec{V}^{\mathrm{R}}_{\alpha'}\right|} = \sqrt{\frac{m_{\alpha'}E^{\mathrm{C}}_{\mathrm{Li}}}{m_{\mathrm{Li}}\varepsilon^{\mathrm{R}}_{\alpha'}}}.
\end{aligned} \tag{8}$$

Note that after the transformation in the first step, the velocity $\vec{V}^{\mathrm{C}}_{\alpha'}$ is still in the x''-y''-z'' coordinate frame. So the second step is to transform the velocity $\vec{V}^{\mathrm{C}}_{\alpha'}$ from the x''-y''-z'' frame to the x'-y'-z' frame. As can be seen from Fig. 2, the x'-y'-z' frame can be rotated to the x''-y''-z'' frame by two rotations: first rotate $-\theta^{\mathrm{C}}_{\mathrm{Li}}$ degrees along the x' axis, and then rotate $(2/\pi-\varphi^{\mathrm{C}}_{\mathrm{Li}})$ degrees along the z' axis. Therefore, the coordinates of the vector $\vec{V}^{\mathrm{C}}_{\alpha'}$ can be transformed from the x''-y''-z'' frame to the x'-y'-z' frame by the matrix operation as follows:

$$\begin{pmatrix} x' \\ y' \\ z' \end{pmatrix} = R_z\left(\frac{\pi}{2}-\varphi^{\mathrm{C}}_{\mathrm{Li}}\right)R_x\left(\theta^{\mathrm{C}}_{\mathrm{Li}}\right)\begin{pmatrix} x'' \\ y'' \\ z'' \end{pmatrix}, \tag{9}$$

where $R_z()$ and $R_x()$ are the unit rotation matrices, which can be expressed as follows:

$$\begin{aligned}
R_z(\theta) &= \begin{bmatrix} \cos\theta & \sin\theta & 0 \\ -\sin\theta & \cos\theta & 0 \\ 0 & 0 & 1 \end{bmatrix},\\
R_x(\theta) &= \begin{bmatrix} 1 & 0 & 0 \\ 0 & \cos\theta & \sin\theta \\ 0 & -\sin\theta & \cos\theta \end{bmatrix}.
\end{aligned} \tag{10}$$

After the transformation of the two steps, the energy and angle of the second emitted particles in the CMS are obtained. Note that there is a one-to-one correspondence for the angle between the first and second emitted particles through the angle information of the intermediate nucleus ^{7}Li.

Finally, the energy and angle of the first and second emitted particles are transferred from the CMS to the LS. The transformation method is the same as that shown as Eq. (8). There is a trick here which can reduce the calculation amount greatly. The final results we want are the energy and angle of the particles in the LS. As can be seen from Fig. 2, the length of the velocity $\vec{V}^{\mathrm{L}}_{\alpha'}$ is independent of the angle $\varphi^{\mathrm{C}}_{\mathrm{Li}}$. On the other hand, as can be seen from Eq. (9), the transformation from the RNS to the CMS is related to the angle $\varphi^{\mathrm{C}}_{\mathrm{Li}}$. Therefore, $\varphi^{\mathrm{C}}_{\mathrm{Li}}$ can be set as a constant, for example, 0°, which can simplify the calculation of the transformation from the RNS to the CMS.

Now the energy and angle of the three particles from the ^{7}Li** or ^{8}Be channels are obtained; thus, the complete final-state phase space is obtained. The probabilities of phase-space bins are calculated by dividing the total cross section of the ^{7}Li** or ^{8}Be channels given by the LUNF code.

IV. CALCULATION METHOD FOR THE BREAKUP CHANNEL

The three-body breakup of the compound nucleus ^{11}B proceeds as a pure kinematic process without interaction between the three particles in the final state. On the basis of energy and momentum conservation, the following equations can be obtained:

$$\begin{aligned}
\varepsilon^{\mathrm{L}}_t+\varepsilon^{\mathrm{L}}_\alpha+\varepsilon^{\mathrm{L}}_{\alpha'} &= E^{\mathrm{L}}_n+Q,\\
\vec{P}^{\mathrm{L}}_t+\vec{P}^{\mathrm{L}}_\alpha+\vec{P}^{\mathrm{L}}_{\alpha'} &= \vec{P}^{\mathrm{L}}_n,
\end{aligned} \tag{11}$$

where E^{L}_n and $\vec{P}^{\mathrm{L}}_n$ are the energy and momentum of the incident neutron in the LS, respectively; Q is the reaction energy of the ^{10}B$(n,t2\alpha)$ reaction. The three particles in the final state include nine degrees of freedom as shown in Eq. (4). Equations (11) contain four constraints, so at least five degrees of freedom need to be set first to decide all of the nine degrees of freedom. The following five quantities are selected:

$$\left(\varepsilon^{\mathrm{L}}_t,\theta^{\mathrm{L}}_t,\varphi^{\mathrm{L}}_t;\theta^{\mathrm{L}}_\alpha,\varphi^{E}_\alpha\right), \tag{12}$$

which are the energy and angle of the triton and the angle of one of the α particles. On the basis of the five initial quantities, the nine degrees of freedom can be obtained by the following three steps.

First, the two α particles in the final state are taken as a whole, which is quasi-2α particle. The energy and angle of

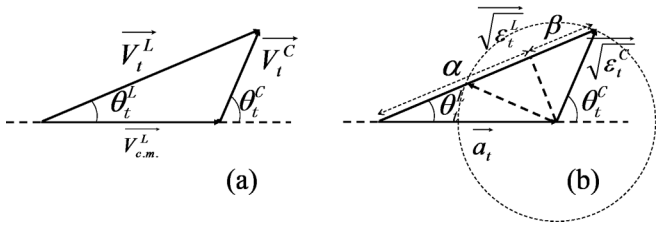

FIG. 3. (a) Velocity triangle and (b) "energy" triangle for the triton from the breakup channel.

the triton in the CMS are related to the energy and angle in the LS through the well-known velocity triangle as shown in Fig. 3(a). Since it is more convenient to work with energies, the velocity triangle can be transformed into an "energy triangle" by multiplying each velocity with $\sqrt{m_t/2}$ as shown in Fig. 3(b) [18]. The quantity m_t is the mass of the triton. In Fig. 3(b), the magnitude of the "energy vector" $\overrightarrow{a_t}$ can be expressed as follows:

$$|\overrightarrow{a_t}| = \sqrt{\frac{1}{2}m_t\left(\left|\overrightarrow{V^{\rm L}_{\rm c.m.}}\right|\right)^2} = \sqrt{\frac{1}{2}m_t\left(\frac{\sqrt{2m_n E^{\rm L}_n}}{M_{10\rm B}+m_n}\right)^2}, \quad (13)$$

where $\overrightarrow{V^{\rm L}_{\rm c.m.}}$ is the velocity of the center of mass in the LS. The triton energy in the CMS, $\varepsilon^{\rm C}_t$, can be calculated using equations similar to Eq. (6).

Using the geometrical relationship of the "energy triangle," the maximum and minimum of the triton energy $\varepsilon^{\rm L}_t$ in the LS can be expressed as follows:

$$\varepsilon^{\rm L}_{t,\,\rm max} = (\alpha+\beta)^2,$$
$$\varepsilon^{\rm L}_{t,\,\rm min} = \begin{cases}(\alpha-\beta)^2, & \alpha > \beta\\ 0, & \alpha \leqslant \beta,\end{cases} \quad (14)$$

where α and β are depicted in Fig. 3(b) and can be expressed as

$$\alpha = |\overrightarrow{a_t}|\cos\theta^{\rm L}_t,$$
$$\beta = \sqrt{\varepsilon^{\rm C}_t - \left(|\overrightarrow{a_t}|\sin\theta^{\rm L}_t\right)^2}. \quad (15)$$

The maximum and minimum of the angle $\theta^{\rm L}_t$ are

$$\theta^{\rm L}_{t,\,\rm max} = \begin{cases}\sin^{-1}\gamma, & \gamma \leqslant 1\\ 180^\circ, & \gamma > 1,\end{cases}$$
$$\theta^{\rm L}_{t,\,\rm min} = 0^\circ, \quad (16)$$

where γ is defined as

$$\gamma = \frac{\sqrt{\varepsilon^{\rm C}_t}}{|\overrightarrow{a_t}|}. \quad (17)$$

As can be seen from Fig. 3(b), when $\gamma \leqslant 1$ the angle $\theta^{\rm L}_t \leqslant 90^\circ$ and the triton energy $\varepsilon^{\rm L}_t$ has double values at each angle of $\theta^{\rm L}_t$ (except the maximum angle $\theta^{\rm L}_{t,\,\rm max}$).

From Eqs. (14) and (16), the range of the energy $\varepsilon^{\rm L}_t$ and angle $\theta^{\rm L}_t$ of the triton can be obtained. In the numerical calculation, the quantities $\varepsilon^{\rm L}_t$ and $\theta^{\rm L}_t$ are discretized. The angle $\varphi^{\rm L}_t$ is independent of the energy $\varepsilon^{\rm L}_t$, and it can be set as a constant. (In the present work, $\varphi^{\rm L}_t$ is set to be 180°.) After the first step, the energy and angle of the triton are obtained.

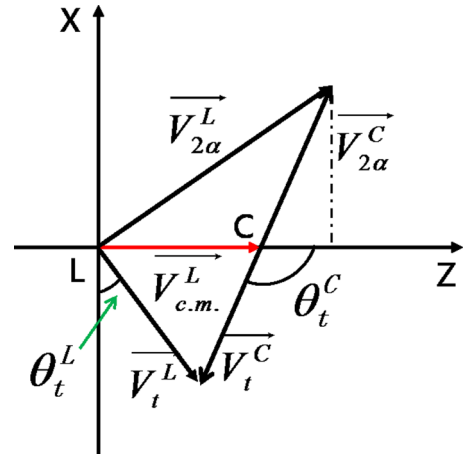

FIG. 4. The relationship of the velocity vector of triton and quasi-2α particle between the CMS and the LS.

The next step is to calculate the energy and angle of one of the two α particles. In the CMS, the triton and the quasi-2α particle move in the opposite direction. Since the angle $\varphi^{\rm L}_t$ is set to be 180°, the angle $\varphi^{\rm L}_{2\alpha}$ is equal to 0°. Therefore, the relationship of the velocity vector of the quasi-2α particle and triton in the LS is simplified in the x-z plane as shown in Fig. 4.

On the basis of the geometrical relationship as shown in Fig. 4, the velocity component of the quasi-2α particle in the LS can be expressed as follows [18]:

$$\left(\overrightarrow{V^{\rm L}_{2\alpha}}\right)_x = \left|\overrightarrow{V^{\rm C}_{2\alpha}}\right|\cdot\cos\left(\theta^{\rm C}_t - 90^\circ\right) = \frac{\sqrt{\left(2m_t\varepsilon^{\rm C}_t\right)}}{m_\alpha + m_{\alpha'}}\sin\theta^{\rm C}_t,$$
$$\left(\overrightarrow{V^{\rm L}_{2\alpha}}\right)_y = 0,$$
$$\left(\overrightarrow{V^{\rm L}_{2\alpha}}\right)_z = \left|\overrightarrow{V^{\rm L}_{\rm c.m.}}\right| + \left|\overrightarrow{V^{\rm C}_{2\alpha}}\right|\cdot\sin\left(\theta^{\rm C}_t - 90^\circ\right)$$
$$= \left|\overrightarrow{V^{\rm L}_{\rm c.m.}}\right| - \frac{\sqrt{\left(2m_t\varepsilon^{\rm C}_t\right)}}{m_\alpha + m_{\alpha'}}\cos\theta^{\rm C}_t, \quad (18)$$

where the energy $\varepsilon^{\rm C}_t$ and angle $\theta^{\rm C}_t$ were obtained in the first step.

In the moving system of the quasi-2α particle, the two α particles move in the opposite direction. The magnitude of the velocity for one of the α particles in the moving system can be expressed as

$$|\overrightarrow{v}| = \sqrt{\frac{2m_{\alpha'}E_{2\alpha}}{m_\alpha(m_\alpha+m_{\alpha'})}},$$
$$E_{2\alpha} = E^{\rm C}_{\rm tot} - \frac{m_t+m_\alpha+m_{\alpha'}}{m_\alpha+m_{\alpha'}}\varepsilon^{\rm C}_t, \quad (19)$$

where $E_{2\alpha}$ is the total kinetic energy of the two α particles in the moving system and $E^{\rm C}_{\rm tot}$ is the total kinetic energy of the three particles in the CMS. The velocity vector $\overrightarrow{v}$ defines a sphere with the center at the end of the velocity vector $\overrightarrow{V^{\rm L}_{2\alpha}}$ as shown in Fig. 5.

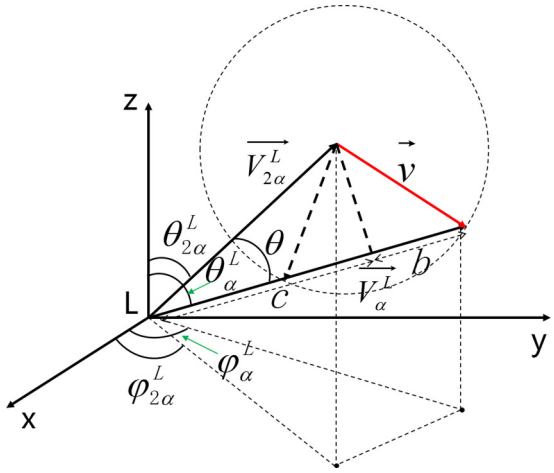

FIG. 5. The relationship of the velocity vector of the α particle between the LS and the quasi-2α particle moving system.

The energy of one of the α particles in the LS can be expressed as follows:

$$\begin{aligned} \varepsilon^{\mathrm{L}}_{\alpha} &= \tfrac{1}{2} m_{\alpha}(c \pm b)^2, \\ b^2 &= |\vec{v}|^2 - \left(\left|\vec{V}^{\mathrm{L}}_{2\alpha}\right|^2 - c^2\right), \\ c &= \left|\vec{V}^{\mathrm{L}}_{2\alpha}\right| \cdot \cos\theta, \end{aligned} \tag{20}$$

where the parameters b and c are shown in Fig. 5. The angle θ is an unknown quantity and it can be expressed using the formula of included angle:

$$\cos\theta = \cos\theta^{\mathrm{L}}_{2\alpha}\cos\theta^{\mathrm{L}}_{\alpha} + \sin\theta^{\mathrm{L}}_{2\alpha}\sin\theta^{\mathrm{L}}_{\alpha}\cos\left(\varphi^{\mathrm{L}}_{2\alpha} - \varphi^{\mathrm{L}}_{\alpha}\right). \tag{21}$$

The meanings of the angles are shown in Fig. 5. The angle $\varphi^{\mathrm{L}}_{2\alpha}$ is equal to 0°.

As shown in Eq. (20), the expression of the quantity b includes the parameter c, so we further define two new quantities as follows:

$$\alpha = c, \quad \beta = b^2 - c^2. \tag{22}$$

Substituting Eqs. (21) and (22) into Eq. (20), the following equations can be obtained [18]:

$$\begin{aligned} \varepsilon^{\mathrm{L}}_{\alpha} &= \tfrac{1}{2} m_{\alpha}(\alpha \pm \sqrt{(\alpha^2 + \beta)})^2, \\ \alpha &= \left(\vec{V}^{\mathrm{L}}_{2\alpha}\right)_x \sin\theta^{\mathrm{L}}_{\alpha}\cos\varphi^{\mathrm{L}}_{\alpha} + \left(\vec{V}^{\mathrm{L}}_{2\alpha}\right)_z \cos\theta^{\mathrm{L}}_{\alpha}, \\ \beta &= |\vec{v}|^2 - \left|\vec{V}^{\mathrm{L}}_{2\alpha}\right|^2. \end{aligned} \tag{23}$$

When $\beta > 0$, the energy $\varepsilon^{\mathrm{L}}_{\alpha}$ has one solution and the sign is positive; when $-\alpha^2 < \beta < 0$, $\varepsilon^{\mathrm{L}}_{\alpha}$ has two solutions; and when $\beta < -\alpha^2$, $\varepsilon^{\mathrm{L}}_{\alpha}$ has no solution.

Using Eq. (23), the energy of one of the α particles is obtained. The angles $\theta^{\mathrm{L}}_{\alpha}$ and $\varphi^{\mathrm{L}}_{\alpha}$ are discretized. After the second step, the energy and angle of one of the α particles are obtained.

In the final step, the energy and angle of the triton and the first α particle are substituted into Eq. (11), and then the energy and angle of the other α particle are obtained.

Now the energy and angle of the three particles from the breakup channel are obtained, and then the complete final-state phase space is obtained. The probabilities of phase-space bins can be calculated using the expression of the triple-differential cross section [18]:

$$\begin{aligned} \frac{d^3\sigma}{d\varepsilon^{\mathrm{L}}_t d\Omega^{\mathrm{L}}_t d\Omega^{\mathrm{L}}_{\alpha}} &= \frac{2\pi}{\hbar^2}\frac{\mu_n}{k_n}\langle|M|\rangle^2\rho\left(\varepsilon^{\mathrm{L}}_t\right), \\ \mu_n &= \frac{m_n m_{10\mathrm{B}}}{m_n + m_{10\mathrm{B}}}, \\ k_n &= \frac{1}{\hbar}\mu_m\left|\vec{p^{\mathrm{L}}_n}\right|/m_n, \end{aligned} \tag{24}$$

where μ_n and k_n are the reduced mass and momentum of the incident neutron. The matrix element $\boldsymbol{M}$ has several forms. For the cross section of a pure statistical energy distribution, like the case of the breakup channel, the matrix element $\boldsymbol{M}$ can be assumed to be a constant. $\rho(\varepsilon^{\mathrm{L}}_t)$ is the density of the final state and it can be expressed as follows [18]:

$$\begin{aligned} &\rho\left(\varepsilon^{\mathrm{L}}_t\right)d\varepsilon^{\mathrm{L}}_t d\Omega^{\mathrm{L}}_t d\Omega^{\mathrm{L}}_{\alpha} \\ &= \frac{h^{-6} m_t m_{\alpha} m_{\alpha'}\left|\vec{p^{\mathrm{L}}_t}\right|\left|\vec{p^{\mathrm{L}}_{\alpha}}\right|}{(m_{\alpha} + m_{\alpha'}) + m_{\alpha}\left(\vec{p^{\mathrm{L}}_t} - \vec{p^{\mathrm{L}}_n}\right)\vec{p^{\mathrm{L}}_{\alpha}}/\left|\vec{p^{\mathrm{L}}_{\alpha}}\right|^2} d\varepsilon^{\mathrm{L}}_t d\Omega^{\mathrm{L}}_t d\Omega^{\mathrm{L}}_{\alpha}, \end{aligned} \tag{25}$$

where $\vec{p^{\mathrm{L}}_n}$, $\vec{p^{\mathrm{L}}_t}$, and $\vec{p^{\mathrm{L}}_{\alpha}}$ are the momenta of the neutron, triton, and the first α particle, respectively. Using Eq. (25), the probabilities of phase-space bins for the breakup channel can be calculated.

V. INTERFERENCE REACTIONS

The interference reactions can be detected by the GIC detector and its spectrum will superimpose on that of the ^{10}B(n,$t2\alpha$) reaction. Three kinds of interference reactions are taken into account: (1) the ^{10}B(n,α)^{7}Li reaction; (2) the elastic scattering reaction between the neutron and hydrogen which are adsorbed in the cathode plate, namely, the H(n, n)p reaction; and (3) the (n,α) reactions of the isotopes in the working gas of the GIC, which include

$$\begin{aligned} n + {}^{13}\mathrm{C} &\rightarrow \alpha + {}^{10}\mathrm{Be} - 3.836\ \mathrm{MeV}, \\ n + {}^{16}\mathrm{O} &\rightarrow \alpha + {}^{13}\mathrm{C} - 2.216\ \mathrm{MeV}, \\ n + {}^{17}\mathrm{O} &\rightarrow \alpha + {}^{14}\mathrm{C} + 1.818\ \mathrm{MeV}, \\ n + {}^{82}\mathrm{Kr} &\rightarrow \alpha + {}^{79}\mathrm{Se} + 0.974\ \mathrm{MeV}, \\ n + {}^{84}\mathrm{Kr} &\rightarrow \alpha + {}^{81}\mathrm{Se} - 0.404\ \mathrm{MeV}. \end{aligned} \tag{26}$$

Although the ^{12}C isotope abundance (98.93%) is much larger than that of the ^{13}C (1.07%) [12], the ^{12}C(n,α)^{9}Be reaction is neglected because of the negative, rather large Q value (−5.702 MeV). There are mainly four stable Kr isotopes, ^{82}Kr, ^{83}Kr, ^{84}Kr, and ^{86}Kr, with abundances of 11.59%, 11.50%, 56.99%, and 17.28%, respectively. The ^{83}Kr(n,α)^{80}Se reaction is not taken into account due to the large Q value (3.416 MeV) and the comparatively low isotope abundance of ^{83}Kr (11.50%); the ^{86}Kr(n,α)^{83}Se reaction is neglected because the cross sections are very small at

$E_n = 4.0 \sim 6.0$ MeV predicted by the TALYS-1.6 code and in the ENDF/B-VII.1 library.

The ^{10}B$(n,p)^{10}$Be reaction would be another interference reaction considering the Q value (0.225 MeV), yet this reaction is neglected for two reasons. First, the pressure of the working gas is not high enough to stop the proton completely, so not all of the energy of the proton is deposited into the working gas and collected by the GIC. The ^{10}B$(n,p)^{10}$Be reaction events will locate below the energy range of the ^{10}B$(n,t2\alpha)$ reaction events. Second, the positions of the proton events in the forward spectrum are taken into account through considering the H(n, n)p reaction. As shown in the second paper [10], the forward spectrum will be used to select the effective events.

All of the interference reactions are two-body reactions, so the calculation method of the final-state phase space is similar to that of the first emitted particle in the ^{7}Li** or ^{8}Be channel. For the ^{10}B$(n,\alpha)^7$Li reaction, the cross sections and the angular distribution of the α particle were calculated by the LUNF code. For the H(n, n)p reaction, the cross sections were obtained from the ENDF/B-VII.1 library and the angular distribution of the recoil proton was assumed to be isotropic in the CMS. For the (n,α) reactions from the working gas, the TALYS-1.6 code was used to calculate the cross sections and the angular distribution of the α particle with default parameters.

VI. THEORETICAL CALCULATION OF THE SPECTRUM

After obtaining the complete final-state phase space of the ^{7}Li**, ^{8}Be, and breakup channels, one can check the self-consistency of all of the phase-space bins. There are three criteria:

(1) The summation of the probabilities of the phase-space bins satisfies the conservation of total cross section.
(2) The energy of the three particles for each phase-space bin satisfies the conservation of energy.
(3) The energy and angle of the three particles for each phase-space bin satisfy the conservation of momentum.

By calculation, we find that all of the phase-space bins satisfy the above three criteria, so the accuracy of the calculated phase space is verified.

By integration of the phase-space bins, the spectra can be obtained which include both one-dimensional (1D) and two-dimensional (2D) spectra. There are two kinds of 1D spectra, the forward and backward anode spectra and the total-energy spectrum. For 2D spectra, there are also two types: the grid versus the anode and the forward anode versus the backward anode.

Figures 6(a) and 6(b) show the forward and backward anode 1D spectra, respectively, for the ^{7}Li**, ^{8}Be, and breakup channels of the ^{10}B$(n,t2\alpha)$ reaction together with the ^{10}B$(n,\alpha)^7$Li reaction at $E_n = 4.0$ MeV. The energy loss of the products in the sample and the wall effect of the sample position well are not included in this figure. In the figure, the curve of $(n, t2\alpha)$ is the summation of the curves of ^{7}Li**, ^{8}Be, and breakup. Since the cross sections of the breakup channel are not given by the LUNF code, their values are set to be equal to those of the ^{7}Li** channel based on the existing experimental results [3,8]. As can be seen from Figs. 6(a) and 6(b), the

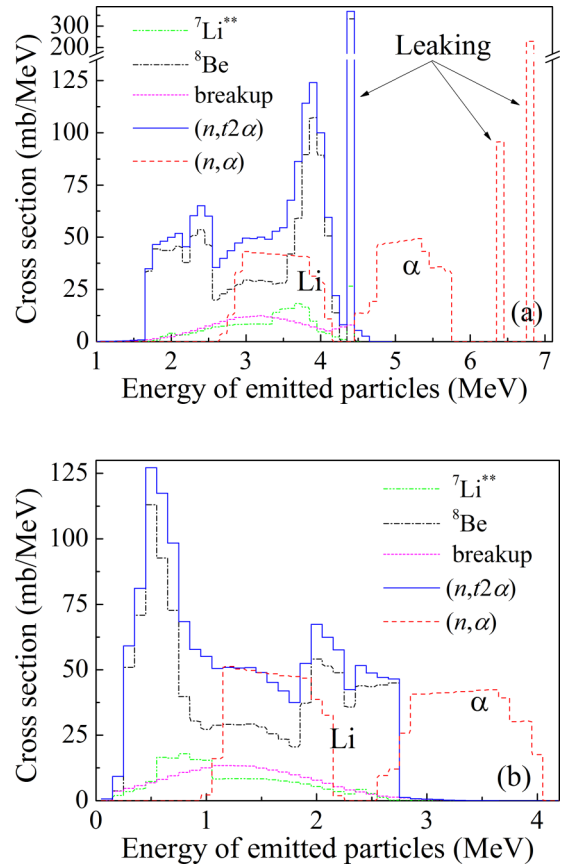

FIG. 6. (a) Forward and (b) backward anode 1D spectra for the ^{10}B$(n,t2\alpha)$ and ^{10}B$(n,\alpha)^7$Li reactions at $E_n = 4.0$ MeV without the corrections of energy loss in the sample and wall effect of the sample position well.

largest contribution to the ^{10}B$(n,t2\alpha)$ reaction is from the ^{8}Be channel. It is worth noting that the relative contributions of the ^{7}Li**, ^{8}Be, and breakup channels are still an open experimental problem.

A noticeable feature of the forward 1D spectrum are the peaks of the so-called leaking events existing in both the ^{10}B$(n,t2\alpha)$ and the ^{10}B$(n,\alpha)^7$Li reactions as shown in Fig. 6(a). This kind of event was first noticed by Georgios *et al.* in 2005 in the measurement of the ^{10}B$(n,\alpha)^7$Li reaction [19]. It was named a leaking event because people ignored such events in the previous experiments. The leaking event is a special kinematic effect occurring in the light-nucleus reaction in that all of the products are emitted in the forward direction. There are two leaking peaks in the spectrum of the ^{10}B$(n,\alpha)^7$Li reaction which correspond to the ground and the first excited states of the ^{7}Li residual nucleus, respectively.

The forward 1D spectra of the ^{7}Li**, ^{8}Be, and breakup channels are very different from each other as shown in Fig. 6(a). For the ^{8}Be channel, in addition to the leaking event peak, there are another two peaks. The peak with higher energy corresponds to such events that the triton is emitted forward. The other peak with lower energy corresponds to that the triton is emitted backward and at least one α particle is emitted forward. The triton in the ^{8}Be channel belongs to

the first emitted particle, so its energy is relatively high. This leads to the fact that the triton events are separated from the α-particle events to some degree in the spectrum of the ^{8}Be channel. For the ^{7}Li** channel, the triton is the second emitted particle with low energy, so the triton cannot be separated from the α-particle events and they become one broad peak. For the breakup channel, the shape of the spectrum is similar to the Gaussian distribution which is a classical result of purely statistical energy distribution. Since the characteristics of the forward spectrum for the ^{7}Li**, ^{8}Be, and breakup channels are different from each other, if the forward spectrum is measured accurately, the proportion of contribution from the ^{7}Li**, ^{8}Be, and breakup channels can be calculated by unfolding the forward spectrum.

The structure of the forward spectrum for the ^{10}B$(n,\alpha)^{7}$Li reaction is relatively simple and clear. The α particle and the recoil ^{7}Li events separate well from each other as shown in Fig. 6(a). The ^{7}Li events overlap with the events of the ^{10}B$(n,t2\alpha)$ reaction, while the α-particle and leaking events separate well from the three-body reaction events because of their higher energy.

Figure 6(b) shows the backward 1D spectrum of the ^{10}B$(n,t2\alpha)$ and ^{10}B$(n,\alpha)^{7}$Li reactions. The energy of the backward events is much lower than that of the forward ones. For the ^{8}Be channel, the peak with higher energy comes from the triton events and the peak with lower energy from the α-particle events. The two peaks correspond one to one with those in the forward spectrum. The structure of the ^{10}B$(n,\alpha)^{7}$Li reaction spectrum is clear. The peaks of the α particle and the recoil ^{7}Li events correspond one to one with those in the forward spectrum. In the backward spectrum, the ^{7}Li events overlap with the three-body reaction events.

Figure 7 shows the spectra of the ^{10}B$(n,t2\alpha)$ and ^{10}B$(n,\alpha)^{7}$Li reactions, taking into account the energy loss in the sample and the wall effect of the sample position well. The main changes of the spectra are that the leaking peaks disappear in the forward spectrum. This is due to the fact that, for the leaking events, the three particles [or two particles for the ^{10}B$(n,\alpha)^{7}$Li reaction] are emitted with large angles. The particles go through a longer path in the sample, and thus the energy loss is larger. In addition, with large emission angle, the particles are more likely to collide with the wall of the sample position well, and thus the energy detected by the GIC becomes lower.

According to the present experimental scheme, the numbers of events for the ^{10}B$(n,t2\alpha)$ and ^{10}B$(n,\alpha)^{7}$Li reactions are obtained from the total-energy 1D spectrum. Figure 8 shows the predicted total-energy 1D spectrum. Before considering the energy loss in the sample and the wall effect of the sample position well, the total-energy 1D spectra of the ^{10}B$(n,t2\alpha)$ and ^{10}B$(n,\alpha)^{7}$Li reactions are actually one and two energy peaks, respectively. This indicates that the final-state phase space satisfies the energy conservation. After considering the two effects, the spectra are broadened. In the total-energy 1D spectrum, the three-body reaction events separate well from those of the two-body reaction.

Figure 9 shows the 2D spectra of the grid versus the anode for the ^{10}B$(n,t2\alpha)$ and ^{10}B$(n,\alpha)^{7}$Li reactions taking into account the energy loss in the sample and the wall effect of the

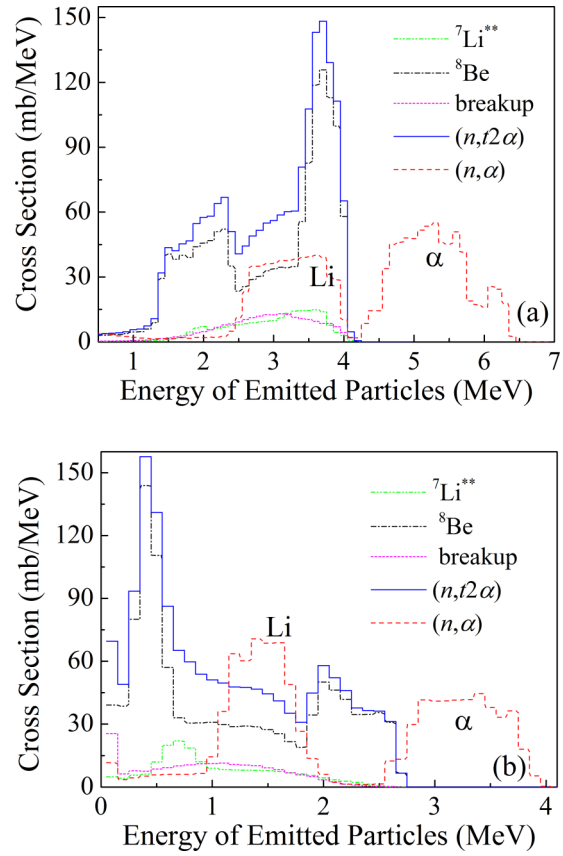

FIG. 7. (a) Forward and (b) backward anode 1D spectra for the ^{10}B$(n,t2\alpha)$ and ^{10}B$(n,\alpha)^{7}$Li reactions at $E_n = 4.0$ MeV after the corrections of energy loss in the sample and wall effect of the sample position well.

sample position well. The spectra of the interference reactions are also plotted in the figure. Here the "energy on grid" ("energy on anode") refers to the energy corresponding to the height of the grid (anode) pulse. The height of the cathode and anode pulse can be calculated using the formulas in Ref. [20], while the height of the grid pulse cannot be calculated by a specific formula. In the present work, a numerical simulation

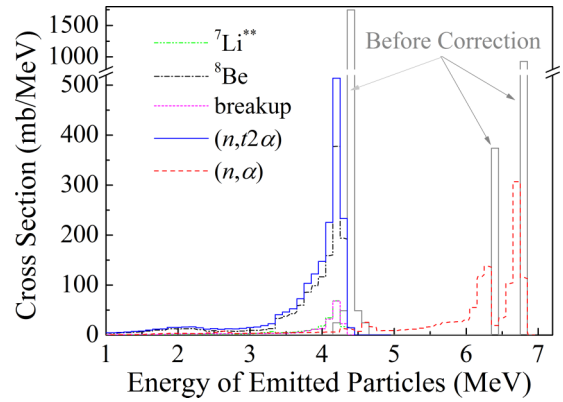

FIG. 8. Total-energy 1D spectrum for the ^{10}B$(n,t2\alpha)$ and ^{10}B$(n,\alpha)^{7}$Li reactions at $E_n = 4.0$ MeV before and after the corrections of energy loss in the sample and wall effect of the sample position well.

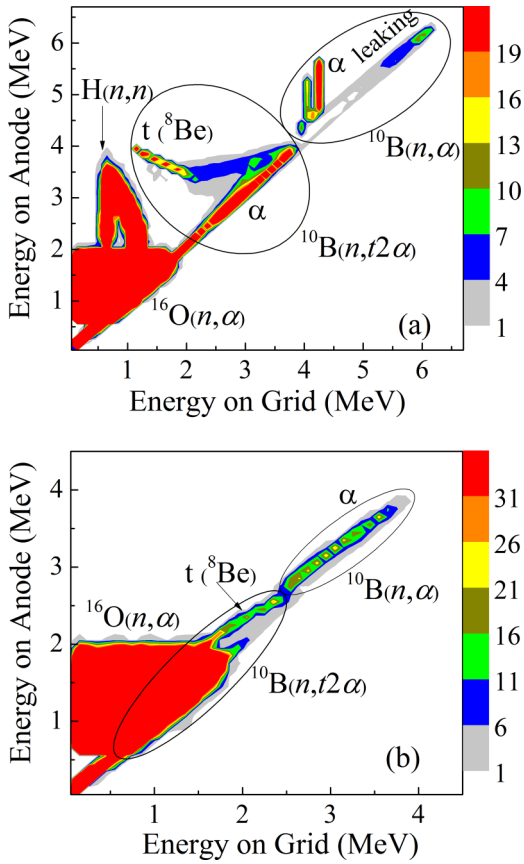

FIG. 9. (a) Forward and (b) backward grid-anode 2D spectrum for the ^{10}B$(n,t2\alpha)$ and interference reactions at $E_n = 4.0$ MeV.

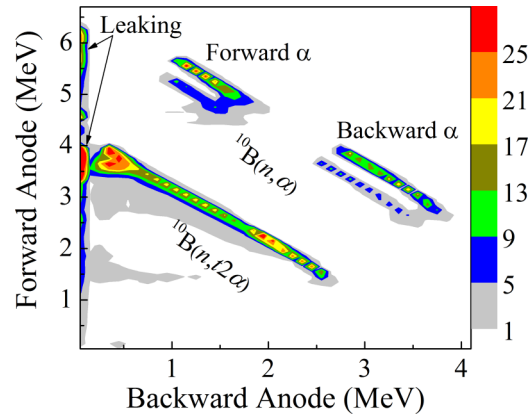

FIG. 10. Backward-forward two-dimensional spectrum for the ^{10}B$(n,t2\alpha)$ and ^{10}B$(n,\alpha)^7$Li reactions at $E_n = 4.0$ MeV.

method was used to calculate the ratios of the grid pulse height to the cathode pulse height based on the law of charge induction on the electrodes. The ratios relate to the energy and directional angle of the incident particles and to the pressure of the GIC. The grid pulse height can be obtained using the simulated ratios and the cathode pulse height. Note that it is helpful to see the following 2D spectra together with the anode 1D spectra as shown in Fig. 7.

In the forward 2D spectrum as shown in Fig. 9(a), the α-particle and leaking events from the ^{10}B$(n,\alpha)^7$Li reaction separate well from the three-body reaction events. On the other hand, there is a certain degree of overlap between the α-particle and leaking events. The distribution structure of the α particle from the ^{10}B$(n,\alpha)^7$Li reaction is vertical, which is correlated with the pressure of the working gas in the GIC. When the gas pressure changes, the length of the ionization track of the α particle changes, and then the amplitude of the grid pulse changes accordingly. In the theoretical calculation, the gas pressures are the same as those used in the experiment which are shown in the second paper [10].

A noticeable characteristic of the forward 2D spectrum for the ^{10}B$(n,t2\alpha)$ reaction comes from the triton events of the ^{8}Be channel shown as "t(^{8}Be)" in Fig. 9(a). Such triton events have large energy, so the corresponding ionization track is long, and thus the amplitude of the grid pulse is low. The distribution of these triton events is slanted, which is due to the kinematic effect of the triton. The larger amplitude of the grid pulse indicates that the emission angle of the triton is larger, while the larger emission angle results in the lower energy. The recoil effect is significant in the light-nucleus reaction due to the light mass.

In the low-energy region of the forward 2D spectrum, the main interference reactions are the H(n,n)p and ^{16}O$(n,\alpha)^{13}$C reactions. Although the energy of the protons is high, the proton events separate well from the three-body events because the amplitudes of the grid pulses are small. In the experimental data processing, the forward 2D spectrum will be used to select the effective events and reduce the influence from the interference events.

Figure 9(b) shows the backward 2D spectrum. Since the energy of the backward events is lower, most events of the ^{10}B$(n,t2\alpha)$ and ^{10}B$(n,\alpha)^7$Li reactions are distributed near the 90° line. The α-particle events from the ^{10}B$(n,\alpha)^7$Li reaction are clear. The triton events from the ^{8}Be channel can be seen to some degree. Since the hydrogen nuclei are considered to be absorbed in the cathode plate and the proton particles from the H(n,n)p reaction emit in the forward direction, there are no H(n,n)p reaction events in the backward spectrum.

Note that the simulated backward spectrum for the (n,α) reactions from the working gas, e.g., the ^{16}O(n,α) reaction events as shown in Fig. 9(b), is different from the measured one. To simplify the calculation process, in the simulation the backward spectrum for the (n,α) reactions from the working gas is calculated independently from the forward one. While in the experiment, the signal sampling of forward and backward pulses is triggered by the forward signal as shown in the second paper, so nearly all of the backward events of the (n,α) reaction from the working gas are discarded. In other words, there are no (n,α) reaction events from the working gas in the experiment.

Figure 10 shows another kind of 2D spectrum which is the backward anode versus the forward anode. The energy summation of the forward and backward signals is equal to the summation of the incident neutron energy and the reaction energy, which can be expressed as

$$E_f + E_b = E_n + Q. \tag{27}$$

The Q values of the ^{10}B(n,$t2\alpha$) and ^{10}B(n,α)^{7}Li reactions are different (0.323 and 2.790 MeV), so the intercepts of the distributions are different in the backward-forward 2D spectrum. The three-body events separate well from the two-body events.

VII. CONCLUSIONS

The ^{10}B(n,$t2\alpha$) three-body reaction proceeds in three ways, namely, the ^{7}Li**, ^{8}Be, and breakup channels. To predict the experimental spectrum of the ^{10}B(n,$t2\alpha$) reaction measured by GIC detector, the complete final-state phase space is calculated for the ^{7}Li**, ^{8}Be, and breakup channels, respectively.

The calculation method of the phase space for the ^{7}Li** and ^{8}Be channels is almost the same. The LUNF code is first used to calculate the angular distribution of the first-emitted particle. The RNS is adopted to calculate the energy and directional angle of the second-emitted particles. A transformation method for the energy and directional angle from the RNS to the CMS is developed by exploiting the rotation properties of the coordinate frames.

The breakup channel proceeds as a pure kinematic process and its calculation method of the phase space is different from that of the ^{7}Li** and ^{8}Be channels. The two α particles are first taken as a whole and the energy and directional angle of the triton are calculated. Then the energy and directional angle of each α particle are calculated, taking full advantage of the relationship of velocity composition between the LS and the moving system of the quasi-2α particle.

Three kinds of interference reactions are taken into account, including the ^{10}B(n,α)^{7}Li reaction, the H(n, n)p reaction, and the (n,α) reactions from the working gas of the GIC (Kr + 2.7% CO_2).

By integration of the phase-space bins, the one-dimensional and two-dimensional spectra are obtained. The energy loss of the products in the sample and the wall effect of the sample position well are considered in the process of integration. The dynamic and kinematic characteristics of the ^{10}B(n,$t2\alpha$) reaction can be seen well from the calculated spectra. The predicted spectra play an important role in the guidance of the implementation of the experiment and the processing of the experimental data.

ACKNOWLEDGMENTS

The authors are grateful to the operation team of the 4.5 MV Van de Graff accelerator of Peking University. Prof. Yinlu Han, Prof. Jingshang Zhang, and Dr. Jimin Wang are acknowledged for the great help in the theory of the neutron induced light-nuclei reaction. The present work was financially supported by the National Natural Science Foundation of China (Grant No. 11475007), China Nuclear Data Center, and the Science and Technology on Nuclear Data Laboratory.

[1] H. J. Taylor and M. Goldhaber, Nature (London) **135**, 341 (1935).
[2] H. J. Taylor, Proc. Phys. Soc. **47**, 873 (1935).
[3] G. M. Frye, J. R. Juanita, and H. Gammel, Phys. Rev. **103**, 328 (1956).
[4] S. M. Qaim and R. Wolfle, Nucl. Phys. A **295**, 150 (1978).
[5] A. Suhaimi, R. Wolfle, S. M. Qaim, and G. Stocklin, Radiochim. Acta **40**, 113 (1986).
[6] V. Valkovic, Nucl. Phys. **54**, 465 (1964).
[7] V. Valkovic, I. Slaus, P. Tomas, and M. Cerineo, Nucl. Phys. A **98**, 305 (1967).
[8] E. A. Davis, F. Gabbard, T. W. Bonner, and R. Bass, Nucl. Phys. **27**, 448 (1961).
[9] T. A. Ivanova, I. P. Bondarenko, B. D. Kuzminov, Y. A. Kurachenko, N. N. Semenova, A. I. Sergachev, and V. A. Khryachkov, Bull. Russ. Acad. Sci.: Phys. **77**, 455 (2013).
[10] Z. Wang, H. Bai, L. Zhang, H. Jiang, Y. Lu, J. Chen, G. Zhang, Y. M. Gledenov, M. V. Sedysheva, and G. Khuukhenkhuu, Phys. Rev. C **96**, 044621 (2017).
[11] J. Zhang, Commun. Theor. Phys. **39**, 433 (2003).
[12] NuDat 2.7β, National Nuclear Data Center, Brookhaven National Laboratory, http://www.nndc.bnl.gov/nudat2/
[13] J. Zhang, Y. Han, and L. Cao, Nucl. Sci. Eng. **133**, 218 (1999).
[14] J. Zhang, Nucl. Sci. Eng. **114**, 55 (1993).
[15] Z. Wang, X. Fan, L. Zhang, H. Bai, J. Chen, G. Zhang, Y. M. Gledenov, M. V. Sedysheva, L. Krupa, and G. Khuukhenkhuu, Phys. Rev. C **92**, 044601 (2015).
[16] H. Bai, Z. Wang, L. Zhang, H. Jiang, Y. Lu, J. Chen, and G. Zhang, Appl. Radiat. Isot. **125**, 34 (2017).
[17] M. B. Chadwick and P. Obloinský, Phys. Rev. C **44**, R1740(R) (1991).
[18] G. G. Ohlsen, Nucl. Instrum. Methods **37**, 240 (1965).
[19] G. Giorginis and V. Khriatchkov, Nucl. Instrum. Methods A **538**, 550 (2005).
[20] A. Gopfert, F.-J. Hambsch, and H. Bax, Nucl. Instrum. Methods A **441**, 438 (2000).